



Supersonically spray-coated copper meshes as textured surfaces for pool boiling

Hong Seok Jo^{a,1}, Min-Woo Kim^{a,1}, Tae Gun Kim^a, Seongpil An^a, Hyun-Goo Park^a, Jong-Gun Lee^a, Scott C. James^b, Jeehoon Choi^{c,*}, Sam S. Yoon^{a,**}

^a School of Mechanical Engineering, Korea University, Seoul 02841, Republic of Korea

^b Depts. of Geosciences and Mech. Eng., Baylor University, Waco, TX 76798, USA

^c LG Electronics Inc., Seoul, Republic of Korea

ARTICLE INFO

Keywords:

Supersonic spraying
Copper nanoparticles
Pool boiling
Superheat temperature
Critical heat flux

ABSTRACT

Pool boiling is a process through which heat is removed upon the vaporization of a coolant fluid surrounding a heated surface and is often applied for cooling high-performance computing systems and nuclear reactors. Increasing the surface-to-volume ratio in confined spaces enhances this cooling method. Here, we introduce textured copper pillars with various geometric arrangements and study their effects on the pool-boiling performance. Frustum pyramids were formed by supersonic spraying copper microparticles through a wire mesh to form pillars of various sizes. We identified an optimal pyramid-base size of 0.91 mm on each side corresponding to the maximum heat transfer coefficient, critical heat flux, boiling heat transfer, and cross-flow coolant velocity over the pyramids. Maximum bubble nucleation was also achieved using this specific geometric arrangement. Such a geometric design can be installed in heat pipe cooling systems to cool electronic devices and nuclear reactors.

1. Introduction

Server computing is an evolving technology that facilitates mobile internet devices and provides entertainment, information, and location-based services in real time. Most server-computing infrastructures offer services delivered through server clusters housed in data centers, which deploy computing hardware comprising high-density chips and high-throughput communication technologies that run software products specifically designed to deliver cloud services. The underlying market trend for data centers is to miniaturize servers, while increasing unit functionality. The resulting increase in heat flux poses enormous challenges for traditional thermal management methods using forced-air convection through finned heat sinks [1–4], which has become problematic, because the power consumption of computer room air conditioning now accounts for approximately 30% of a data center energy consumption [5–7].

Other technologies such as loop heat pipes, water cooling and immersion cooling, are receiving attention [4,8–14]. Loop heat pipes enhance air cooling, but have drawbacks associated with complicated fabrication and integration leading to high costs [15–17]. As opposed to

air cooling, water cooling is less influenced by the ambient temperature inside the servers and thus cooling-energy requirements can be reduced. However, disadvantages include potential leakage, corrosion, significant weight, and the power required to pump water [18]. As an alternative, immersion cooling is highly efficient because it takes advantage of the direct contact between a heated surface and the coolant, as well as the large enthalpy of the corresponding phase change. For example, as depicted in Fig. 1, immersion cooling is not limited to one component, but can simultaneously cool entire systems, including CPUs/GPUs, RAM, power-supply units, and other components. Because this is a relatively complicated and expensive solution, immersion cooling has been a niche technology, used for high-power electronics applications such as military radar systems and high-speed trains [19]. Nevertheless, because thin server-rack units are only 4.3-cm-thick with heat loads of 210–300 W [20], the immersion cooling is well-suited to data-center applications.

Heat transfer for immersion cooling leverages pool boiling, which can be optimized by increasing the critical heat flux (CHF) and the heat transfer coefficient (HTC). Nano-scale geometries employing surface texturing have been shown to enhance CHF and HTC in pool-boiling

* Corresponding author.

** Corresponding author.

E-mail addresses: choijeehoon@gmail.com (J. Choi), skyoona@korea.ac.kr (S.S. Yoon).

¹ These authors have equally contributed.

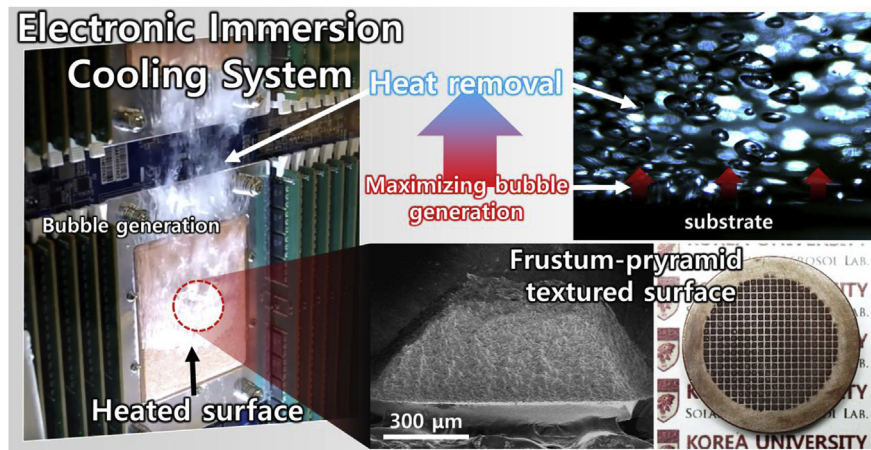


Fig. 1. Immersion cooling system.

applications [21–23]. In previous studies from this group, several nano-texturing methods have been demonstrated to enhance the CHF and HTC by separating liquid and vapor paths, ensuring sufficient liquid flow to cool a surface [24–27]. However, there remain challenges before nano-texturing can become a commercially viable method for the immersion cooling of electronics. To investigate the best approach for immersion cooling, this paper suggests a new nano-texturing technique using a metal-mesh mask and supersonic cold spray, which can be rapidly and scalably implemented. Texturing conditions and configurations are studied to identify nano-texturing structures that facilitate the effective release of bubbles from nucleation sites while providing a sufficient liquid supply to support rapid vaporization rates at high heat loads.

2. Experimental setup

2.1. Materials

Frustum pyramid-shaped pillars were constructed from 1- μm copper powder particles (LeesChem Co., Korea) [28]. The coolant was HFE-7100 (NovecTM Engineering Fluid, 3M), which does not deplete the ozone and is many used in industrial applications including vapor degreasing and the cleaning of co-solvent parts because of its chemical and thermal stability, high vaporization heat, and low toxicity. The thermo-physical properties of the coolant are listed in Table 1 [29].

2.2. Micro-patterned frustum-pyramidal structure coating process

Supersonic cold spraying was used to uniformly pattern copper substrates with frustum-pyramidal pillars. The supersonic cold spray set up and mechanisms for forming the frustum pyramids are described in detail elsewhere [28].

Fig. 2a illustrates the coating process. The metal mesh consisted of wires ($d = 0.4 \text{ mm}$) forming a $50 \times 50 \text{ mm}^2$ mesh mask. Supersonic spraying was implemented using a compressor pressure of 6 bar at

$320 \text{ }^\circ\text{C}$. The distance between the nozzle and substrate was 55 mm. Cu particles were supplied through a powder feeder to coat the substrate, at a volumetric flowrate of $25 \text{ m}^3/\text{min}$. The nozzle was fixed, while the substrate was maneuvered at a speed of 35 mm/s. When the Cu particles collided with the substrate, their kinetic energy was converted into thermal, bonding, and adhesion energies [30]. The Cu particles adhered to the substrate effectively, and underlying particle layers and the frustum pyramid pillars exhibited no detachment from the substrate after several pool-boiling tests.

2.3. Pool-boiling setup

The experimental setup for pool boiling, illustrated in Fig. 3, comprised the test chamber, a Teflon case, an aluminum rod, four heaters, three thermocouples, a Cu substrate with a length (L_{Cu}) of 10 mm and diameter (D_{Cu}) of 30 mm, three preheaters, and a coolant thermocouple. The condensation unit was composed of a chiller and a spiral glass tube.

A power supply (Slidac, 1 kV A, Dae Kwang Electric Co.) transferred heat to the aluminum rod, which has a length (L_{Al}) of 100 mm and diameter (D_{Al}) of 50 mm, with $k_{\text{Al}} = 210 \text{ W m}^{-1} \text{ K}^{-1}$, whose temperature was measured using three thermocouples (Omega Inc.) with accuracies of $\pm 0.3 \text{ }^\circ\text{C}$. These thermocouples were monitored using a data recorder (Memory HiLogger, LR 8400, HIOKI) at three different vertical locations, spaced 8 mm apart, as shown in Fig. 3. The aluminum rod was enclosed in a Teflon case ($k = 0.25 \text{ W m}^{-1} \text{ K}^{-1}$) to minimize heat loss. Thermal grease (Dow Corning, TC-5026, $k_g = 2.89 \text{ W m}^{-1} \text{ K}^{-1}$) was used to fix the sample and reduce the contact thermal resistance between the sample and the aluminum rod.

The coolant was preheated to $60 \text{ }^\circ\text{C}$ using three 100-W preheaters. The condensation unit circulated cooling water at $5 \text{ }^\circ\text{C}$ through a spiral tube carrying water from the chiller (AP15R-30-V11B, VWR Ad). The bottom heaters of the aluminum rod were supplied with a power of 150 W to heat the entire rod and Cu substrate. When the coolant temperature did not change by more than $\pm 0.1 \text{ }^\circ\text{C}$, pool boiling tests were initiated by increasing the thermal output by 15 W every 10 min.

2.4. Characterization

Cross sections of the Cu frustum-pyramid pillars were measured using a field-emission scanning electron microscope (FE-SEM, S-5000, Hitachi) at 15 kV. Snapshots from a CCD camera (Phantom 9.1, Vision Research Inc.) were used to measure capillary phenomena upon the sample being dipped into the coolant and bubble formation being observed. Capillary rises and contact angles in the snapshots were analyzed using a measurement solution (I'MEASER 3.0, ING. PLUS).

Table 1

Thermo-physical properties of HFE-7100.

Physical properties	HFE-7100 (0.1 MPa)
Boiling point ($^\circ\text{C}$)	61
ρ_l (kg m^{-3})	1370.2
ρ_g (kg m^{-3})	987
μ_l ($\text{kg m}^{-1} \text{ s}^{-1}$)	3.70×10^{-4}
σ_{lg} (N m^{-1})	1.019×10^{-2}
c_p ($\text{J kg}^{-1} \text{ K}^{-1}$)	1255
h_{fg} (J kg^{-1})	111.6

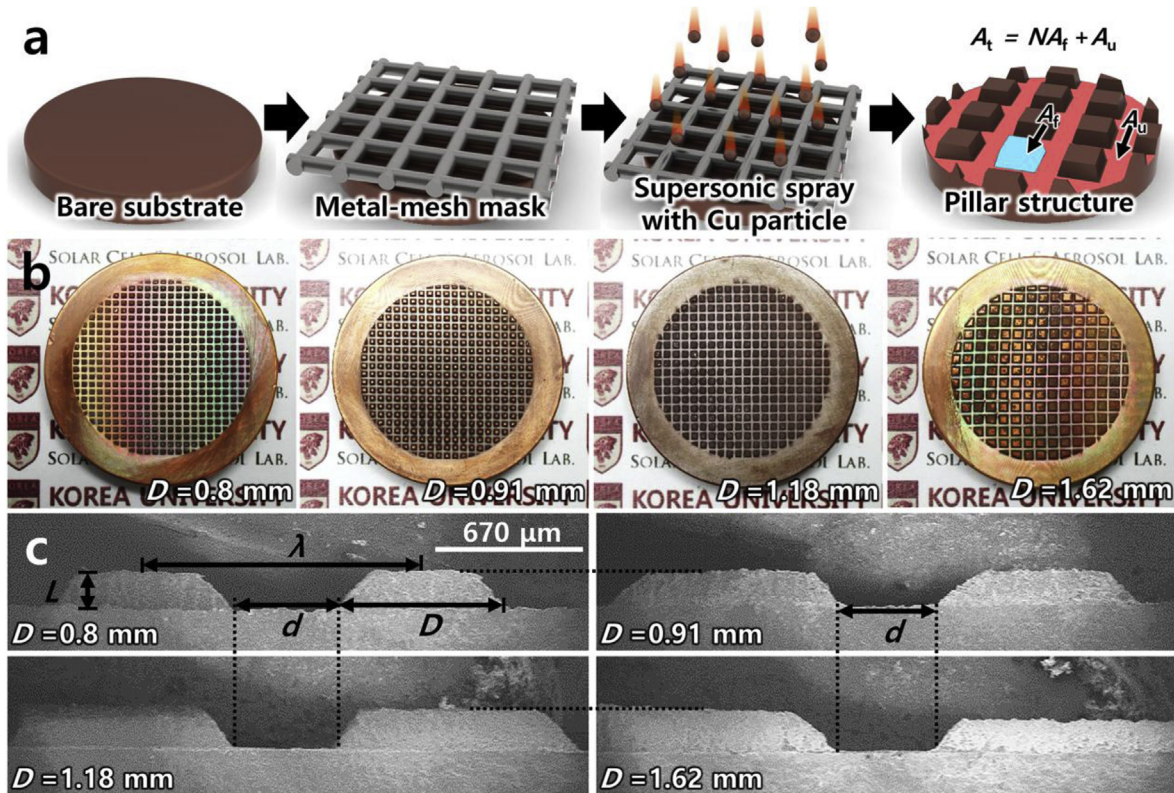


Fig. 2. (a) Schematic of the manufacturing process for the frustum-pyramid pillars on Cu substrates using supersonic cold spraying. (b) Photographs and (c) cross-sectional SEM images for pyramid base lengths of $D = 0.8, 0.91, 1.18,$ and 1.62 mm .

3. Results and discussion

3.1. Frustum-pyramidal structures

Morphologies resulting from the various mesh masks are shown in Fig. 2b and c. As observed in the cross-sectional SEM images in Fig. 2c, pillars were shaped as frustum pyramids, because recirculation zones at mask edges hinder the depositing of Cu particles at boundaries between the mask and substrate [28]. Therefore, as more Cu particles were sprayed they accumulated toward the center to form frustum pyramids.

In this study, the textured surface was generated using two spray passes, and was subsequently filed with sand paper to adjust the pillar height to $L = 130 \mu\text{m}$. The gap between pillars, d , was fixed using a

mesh formed from wire with a diameter of 0.4 mm , although the distance between mesh wires, D , was varied to investigate its impact on cooling performance. As D increased from 0.8 to 1.62 mm , the distance between pillar centers, λ , increased from 1.2 to 2.05 mm . Although D and λ simultaneously increased, the total textured surface coverage area decreased from 15.1% to 11.3% because the number of pillars decreased. The frustum pyramid characteristics are listed in Table 2 along with a description of each experimental case. The pyramid base perimeter is denoted by P .

3.2. Data validation

The heat flux, q'' , from the sample to the coolant was estimated by

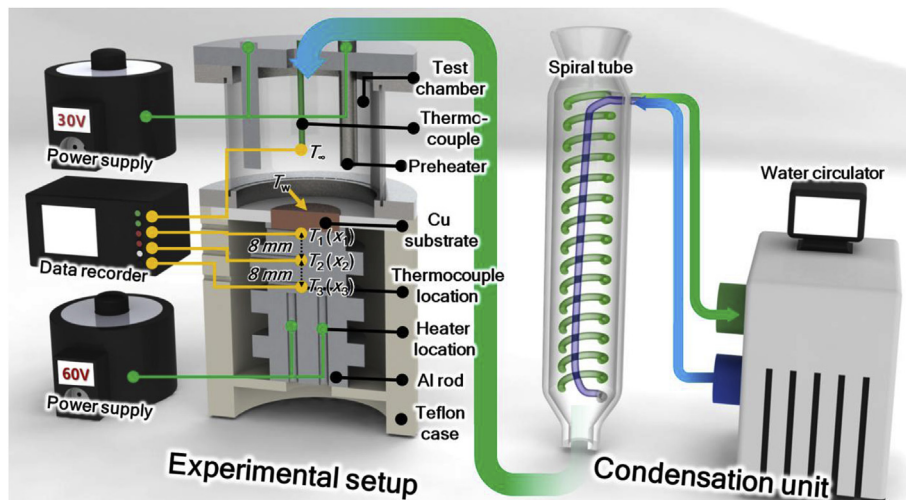


Fig. 3. Schematic of the pool boiling setup, including the condensation unit.

Table 2
Frustum pyramid geometric properties for each experimental Case.

Case	λ [mm]	d [mm]	D [mm]	L [mm]	Surface-area coverage [%]	P [mm]	m [m ⁻¹]	A_f [mm ²]	A_u [cm ²]	N	A_t [cm ²]
1	1.2	0.4	0.80	0.13	15.1	3.2	432	1.06	0.44	1336	14.6
2	1.35	0.4	0.91	0.13	12.7	3.6	407	1.28	3.23	712	12.3
3	1.53	0.4	1.18	0.13	12.3	4.7	356	2.01	2.11	495	12.0
4	2.05	0.4	1.62	0.13	11.3	6.4	305	3.39	2.57	251	11.1

measuring the heat flux through the aluminum rod ($k_{Al} = 210 \text{ W m}^{-1} \text{ K}^{-1}$) using Fourier's law (steady state, one-dimensional):

$$q'' = k_{Al} \frac{T_2 - T_1}{\Delta x_{12}} = k_{Al} \frac{T_3 - T_2}{\Delta x_{23}} = \frac{T_1 - T_w}{\Delta x_g/k_g - \Delta x_w/k_{Cu}}, \quad (1)$$

where Δx_g and Δx_w are the thickness of the thermal grease layer and the distance between x_1 and the surface of the substrate, respectively, and k_g and k_{Cu} are the thermal conductivities of the thermal grease and Cu substrate ($k_{Cu} = 401 \text{ W m}^{-1} \text{ K}^{-1}$), respectively. Three equidistant temperatures (T_1 , T_2 , and T_3 in Fig. 3) were measured at x_1 , x_2 , and x_3 from the middle of the rod, and the distances between the thermocouples were $\Delta x_{12} = \Delta x_{23} = 8 \text{ mm}$. The wall temperature, T_w , was calculated using the preceding equation as:

$$T_w = T_1 - k_{Al} \frac{(T_2 - T_1)}{\Delta x_{12}} \left(\frac{\Delta x_g}{k_g} + \frac{\Delta x_w}{k_{Cu}} \right). \quad (2)$$

Δx_g was measured 10 times using an electronic Vernier caliper (BDJK-565, with a resolution of 0.005 mm and limit error of $\pm 0.015 \text{ mm}$), and the maximum and minimum thicknesses were 0.011 and 0.1 mm, respectively. In (2), the superheat is $\Delta T_{sat} = T_w - T_f$, where T_f is the saturated temperature of the coolant. Finally, the effective heat transfer coefficient, h_{eff} , was estimated using Newton's Law of Cooling as:

$$h_{eff} = \frac{q''_t}{\Delta T_{sat}}. \quad (3)$$

To confirm the reliability of the pool boiling test, experimental results using an uncoated substrate are compared in Fig. 4a to the Rohsenow equation (strictly applicable to a smooth surface) modified to [31,32]:

$$\Delta T_{sat} = \frac{C_{s,f} h_v Pr_l^n}{c_p} \left(\frac{q''_t}{\mu_l h_v} \right)^{1/3} \left[\frac{\sigma}{g(\rho_l - \rho_v)} \right]^{1/6}, \quad (4)$$

where h , Pr , and c_p are the enthalpy of vaporization, Prandtl's number, and specific heat, respectively. Subscripts (_l) and (_v) denote liquid and vapor states, respectively, and μ , σ , ρ , and g are the coolant viscosity, surface tension, density, and gravitational acceleration, respectively. The experimental constant, $C_{s,f}$, depends on the substrate, and liquid materials and experimental data were matched by setting $C_{s,f} = 0.72$ with $n = 1.7$ for the coolant [33].

The uncertainty was estimated using an error-propagation method [34]:

$$U_{q''} = \sqrt{\left(\frac{\partial q''}{\partial V} U_V \right)^2 + \left(\frac{\partial q''}{\partial I} U_I \right)^2 + \left(\frac{\partial q''}{\partial A_{Cu}} U_{A_{Cu}} \right)^2 + \left(\frac{\partial q''}{\partial W_{Te}} U_{W_{Te}} \right)^2}, \quad (5)$$

where V , I , A_{Cu} , and W_{Te} are the voltage, current, substrate surface area, and thickness of the Teflon cylinder, respectively, and the $U_{(\)}$ terms are the uncertainties in the current, voltage, substrate surface area, and thickness of the Teflon cylinder, respectively. In (5), the uncertainty in the heat flux was $\pm 4.5\%$. The temperature measurements were estimated to have an accuracy of $\pm 0.06^\circ \text{C}$, and the uncertainty in the average heat transfer coefficient was about $\pm 3.5\%$.

3.3. Pool boiling heat transfer analysis

Fig. 4b illustrates the relation between q'' and ΔT_{sat} for the uncoated and patterned surfaces. CHF for the uncoated substrate was 189 kW m^{-2} and this increased for all patterned surfaces with a maximum value of 285 kW m^{-2} for Case 2 ($D = 0.91 \text{ mm}$). CHF increased with increasing D up to 0.91 mm , but decreased to 246 kW m^{-2} when $D = 1.62 \text{ mm}$.

As with the trend in CHF, Fig. 4b shows that ΔT_{sat} was lowest for $D = 0.91 \text{ mm}$ and h_{eff} varied for variations in ΔT_{sat} as shown in Fig. 4c, and h_{eff} attained a maximum of $20.2 \text{ kW m}^{-2} \text{ K}^{-1}$ when $D = 0.91 \text{ mm}$. Clearly, CHF and h_{eff} were sensitive to D , demonstrating that the heat transfer depends on pillar geometry. The heat flux of the micro/nano structure was higher than that of the frustum pyramid structure, because of the added nucleation sites and cavities of the micro/nano structure. In addition, for the frustum pyramid structure the generated bubbles easily detached from the surface while embryonic bubbles formed within the pores were hindered from escaping the micro/nano structure. As a result, the h_{eff} values for the frustum pyramid structures were at least as high as those for the micro/nano structure even though the Cu substrate was larger in this study (see Table 4).

As shown in Fig. 4b and c, the boiling heat transfer (BHT) varied as a function of D . The question arises of whether the increase in BHT was primarily due to the increase in surface area or because of the frustum pyramid shapes themselves. Assuming single-phase convective heat transfer, the heat transfer from the patterned surfaces was estimated assuming a fin effect. In this study, the frustum-pyramid pillars were arranged uniformly, so that the fin efficiency of a single pillar (η_{sp}) can be described as [31]:

$$\eta_{sp} = \frac{\tanh mL_c}{mL_c}, \quad (6)$$

where

$$m = \sqrt{\frac{h_u P}{k_{Cu} A_c}}, \quad (7)$$

and h_u , P , and A_c are the heat transfer coefficient for the uncoated surface at CHF, the pillar perimeter, and the projected flow-facing area of the pillar, respectively. Furthermore, L_c is defined as $L + D/2$, h_u and k_{Cu} are constants, and m depends on P and A_c . As D decreased, m decreased from 70.7 to 50 m^{-1} , while η_{sp} decreased from 0.96 to 0.91 (Tables 1 and 2 and Fig. 4d). The increase in η_{sp} for decreasing D was attributed to the increased heat transfer area per unit substrate area.

However, the single fin efficiency is not the best metric for assessing overall performance. Instead, the total efficiency, η_t , which includes the effects of the pillar arrangement, can be considered. The total heat transfer was [31]:

$$q_t = N \eta_{sp} h_u A_f \Delta T_{sat} + h_u A_u \Delta T_{sat} = h_u A_t \left[1 - \frac{N A_f}{A_t} (1 - \eta_{sp}) \right] \Delta T_{sat}, \quad (8)$$

where N is the number of pillars, A_f is the surface area of a single pillar, and A_u is the area without pillars (see Fig. 2a). The total surface area was $A_t = N A_f + A_u$, which combined with $\eta_t = q_t / h_u A_t \Delta T_{sat}$ yields:

$$\eta_t = 1 - \frac{N A_f}{A_t} (1 - \eta_{sp}). \quad (9)$$

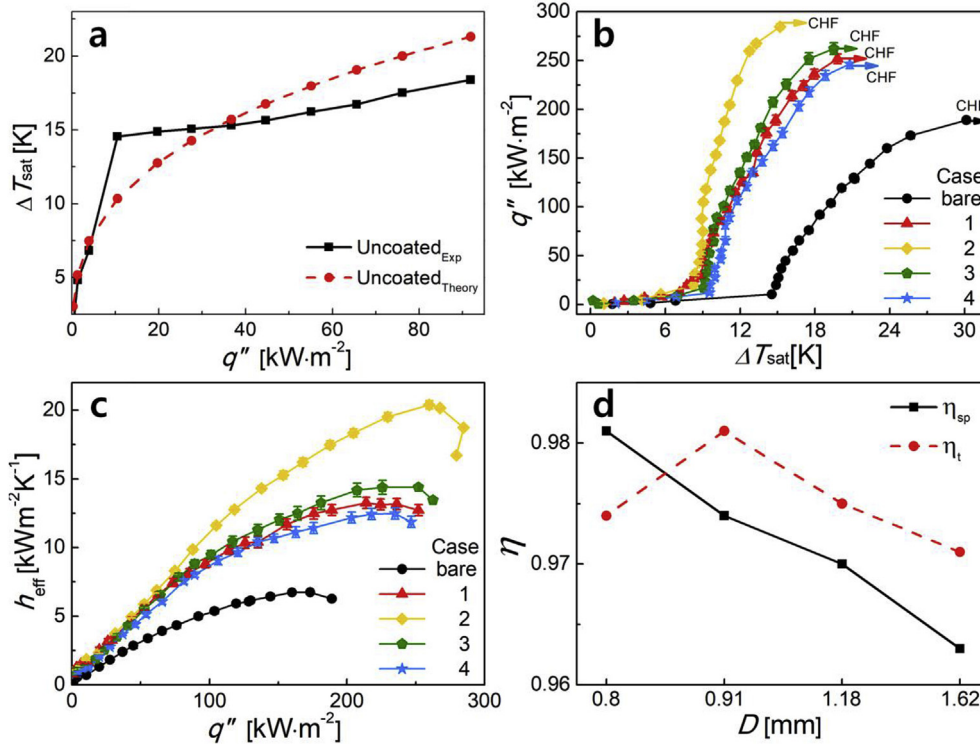


Fig. 4. (a) Comparison of the experimental and theoretical q'' for an uncoated substrate. (b) q'' versus ΔT_{sat} and (c) h_{eff} versus q'' for Cases 1–4 (see Tables 2 and 3). (d) Single-fin and total efficiencies as functions of D .

In the preceding equation, η_t is a function of each parameter, and the optimal point is shown in Fig. 4d. Although A_f and η_{sp} decreased as D increased, N and A_t increased, and η_t attained its maximum at $D = 0.91$ mm according to (9). This demonstrated that there was an optimal pillar size. Considering only a single pillar, the heat transfer increased for smaller D , because η_{sp} increased as D decreased. However, considering all pillars η_t was highest at 0.981 when $D = 0.91$ mm. As a result, the most heat was dissipated when $D = 0.91$ mm and CHF was also highest for $D = 0.91$ mm.

In addition, bubble formation was different for each case. At $\Delta T_{sat} = 7$ °C (the first row of Fig. 5), bubble sizes when $D = 0.91$ mm were slightly bigger than for both the uncoated case and that with $D = 1.62$ mm. More bubbles were also generated for $D = 0.91$ mm. With increasing ΔT_{sat} , bubble formation when $D = 0.91$ mm was further distinguished from the other cases because more coolant circulated when $D = 0.91$ mm. It is seen from Fig. 4d that η_t attained its maximum when $D = 0.91$ mm. Similarly, from Fig. 5, the greatest number of bubbles was observed when $D = 0.91$ mm. This pattern indicated that the optimal η_t value resulted in the highest bubble formation.

3.4. Effects of D on wettability and coolant flow rate

Rewetting is important for cooling hot spots, and is crucial to heat pipe performance [35]. The coolant contact angle, θ , was measured through the capillary rise. Samples were dipped vertically in the coolant and the horizontal capillary rise, t , was measured. Here, θ was

Table 4

Variation of the CHF and h_{eff} values from previous studies with varying substrate materials, shape, and size (d). All working fluid are HFE-7100.

Material	Structure	A [cm ²]	CHF [kW·m ⁻²]	h_{eff} [kW·m ⁻² K ⁻¹]	Ref.
Copper	Micro-porous copper	0.2	450	18	[42]
Copper	Porous graphite	1	320	20	[43]
Si	Mesh	12	220	15	[44]
Si	Micro-cavity on Si	1	300	8	[45]
Copper	Frustum-pyramid	27	285	20	Present

calculated by integrating the Laplace equation over a cylindrical liquid surface as [36,37]:

$$\theta = \sin^{-1} \left(1 - \frac{\Delta \rho g t^2}{2\sigma} \right). \quad (10)$$

The capillary rise increased from $t = 1.08$ – 1.35 mm as D decreased, and the theoretical value of θ decreased from 16.1° to 5.6° as illustrated by the dotted curve in Fig. 6a. The theoretical and measured trends in θ were similar indicating an increased wettability for smaller D .

Wettability is related to the flow rate between pillars by the capillary pressure and friction pressure drop [35,38,39]. The balance for the

Table 3

Experimental conditions and results for each Case.

Case	η_{sp}	η_t	t [mm]	θ_{theory} [°]	θ_{exp} [°]	u_w [m·s ⁻¹]	Nu	Re	V [m·s ⁻¹]
1	0.981	0.974	1.35	5.6	9	0.258	170	8973	1.04
2	0.974	0.981	1.18	12.2	15.5	0.255	270	18,760	1.79
3	0.970	0.975	1.1	15.3	16.7	0.254	274	18,967	1.14
4	0.963	0.971	1.08	16.1	19.8	0.252	295	21,330	0.75

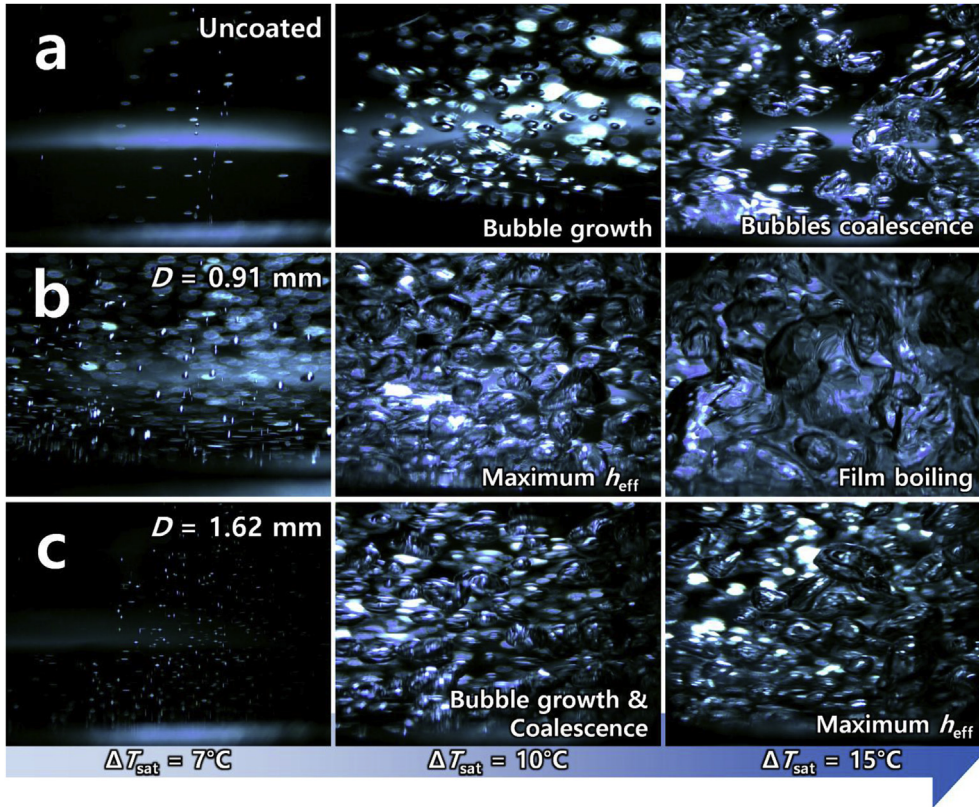


Fig. 5. Snapshots of pool boiling for (a) the uncoated case, and when $D =$ (b) 0.91 and (c) 1.62 mm for $\Delta T_{sat} = 7, 10, \text{ and } 15^\circ\text{C}$ (across columns).

pressure drop is:

$$\frac{2\sigma \cos \theta}{d} - \frac{\mu_1}{\kappa} u_w L = \frac{1}{2} \rho_1 u_w^2, \quad (11)$$

where κ is the permeability of the patterned surface and u_w is the wetting velocity or flow speed through the pillars. The permeability was estimated as:

$$\kappa = \frac{d^2 \varepsilon^2}{36 C_p (1 - \varepsilon)} \approx \frac{d^2 \varepsilon^2}{36 (1 - \varepsilon)}, \quad (12)$$

where C_p and ε are the surface-factor constant and porosity, respectively [38]. The porosity of the patterned surface was $\varepsilon = 1 - (D/\lambda)^2$,

which increased as D decreased. The flow velocity between pillars was calculated as:

$$u_w = \sqrt{\frac{2\sigma \cos \theta}{d} + \frac{\mu_1 L}{\kappa \rho_1}} - \frac{\mu_1 L}{\kappa \rho_1}. \quad (13)$$

In Fig. 6b, the velocity increased as D decreased because $\cos \theta$ (the capillary pressure) increased. The capillary pressure (the first term under the square root in the preceding equation) increased when D decreased. Interestingly, the friction pressure drop (the last term, after the minus sign) also increased when D decreased, because κ decreased. The net magnitude of (13) shows that u_w increased when D decreased, because the capillary pressure term dominated the friction pressure drop.

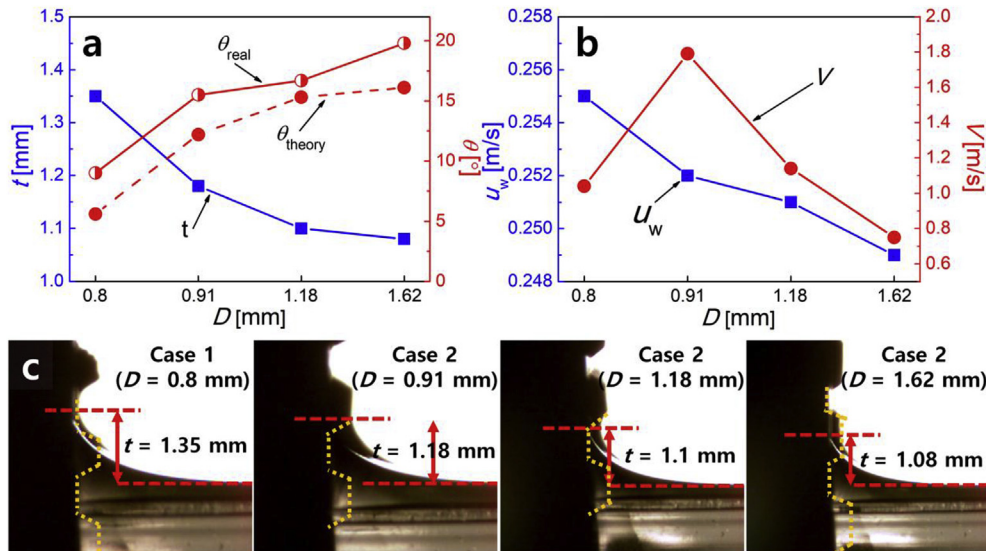


Fig. 6. (a) Capillary heights, and comparison between the experimental and theoretical values of θ for the coolant due to capillary effects and wicking. (b) The cross-flow coolant velocities over the pillars as a function of D . (c) Photographs of capillary heights for D of 0.8–1.62 mm. The dotted curves indicate the coated frustum pyramid structure.

Although the wettability and coolant velocity along the patterned surface helped to saturate dry areas, the overall phenomena of BHT was also described by another parameter: the coolant cross-flow velocity, V , over the pillars. Using the Nusselt number, defined as $Nu = h_{\text{eff}} D/k_l$ where k_l is the conductivity of the coolant, the Reynolds number was [31,40,41]:

$$Re = \left[\frac{Nu}{C \cdot Pr^{0.36}} \cdot \left(\frac{Pr_s}{Pr} \right)^{1/4} \right]^{1/\beta}, \quad (14)$$

where C and β are adjustable parameters and the values of Pr and Pr_s are the same, because the fluid viscosity was constant at a specific temperature. V was estimated using $Re = \rho V_{\text{max}} D / \mu$ and $V_{\text{max}} = \lambda V / (\lambda - D)$, where V_{max} was the maximum flow speed over the pillars:

$$V = \frac{\mu(\lambda - D)}{\rho \lambda D} Re. \quad (15)$$

For decreasing D , h_{eff} was 13.2, 18.7, 14.4, and 11.5 kW m⁻² K⁻¹ at $\Delta T_{\text{sat}} = 15$ K, even though Nu and Re increased with D regardless of h_{eff} as shown in Table 3. However, V attained a maximum of 1.79 m/s at $D = 0.91$ mm as shown in Fig. 6b, which indicates that the cross-flow velocity plays an important role in increasing the pool boiling performance. Although hot spots were rapidly rewetted as D decreased, because u_w increased when bubbles were generated at the hot spot, the overall heat transfer was more strongly correlated to V . Therefore, heat was rapidly transferred at $D = 0.91$ mm, similarly to the effects on h_{eff} shown in Fig. 4c.

4. Conclusion

In this study, we applied a new nano-texturing coating method, to manufacture copper frustum pyramids as commercially viable structures for pool boiling enhancement. Various configurations of copper frustum pyramids were constructed using metal-mesh masks. The pool boiling characteristics for surfaces coated with these pillars were studied, and the optimal mesh size ($D = 0.91$ mm) was identified after comparing all h_{eff} and CHF values. The maximum bubble formation was also observed at this optimal value of D . The total heat transfer efficiency, which was maximum for $D = 0.91$ mm, included the effects of the overall pillar arrangement. The wetting velocity was maximized when D was smallest. However, the cross-flow velocity was largest for $D = 0.91$ mm, which optimized pool boiling. Clearly, the geometric arrangement played an important role in the overall pool boiling performance and the geometric parameters should be designed carefully to optimize the pool boiling performance.

Acknowledgement

This research was supported by the Technology Development Program to Solve Climate Changes of the National Research Foundation (NRF) funded by the Ministry of Science, ICT and Future Planning (NRF-2016M1A2A2936760, NRF-2017R1A2B4005639, and NRF-2013R1A5A1073861). This work was also supported by the National Research Council of Science & Technology (NST) grant by the Korea government (MSIP) (No. CRC-16-02-KICT).

References

- [1] B. Nagendran, S. Nagaraj, J. Fernandes, R. Eiland, D. Agonafer, V. Mulay, Improving cooling efficiency of servers by replacing smaller chassis enclosed fans with larger rack-mount fans. *Thermal and Thermomechanical Phenomena in Electronic Systems (ITherm)*, IEEE Intersociety Conference on. IEEE2014, 2014, pp. 574–582.
- [2] B. Fakhim, M. Behnia, S. Armfield, N. Srinarayana, Cooling solutions in an operational data centre: a case study. *Appl. Therm. Eng.* 31 (2011) 2279–2291.
- [3] K. Ebrahimi, G.F. Jones, A.S. Fleischer, A review of data center cooling technology, operating conditions and the corresponding low-grade waste heat recovery opportunities. *Renew. Sustain. Energy Rev.* 31 (2014) 622–638.
- [4] A.C. Kheirabadi, D. Groulx, Cooling of server electronics: a design review of existing technology. *Appl. Therm. Eng.* 105 (2016) 622–638.
- [5] J.G. Koomey, Estimating Total Power Consumption by Servers in the US and the World, (February 2007).
- [6] A.D. Series, Best practices for DataCom facility energy efficiency, (2009) Atlanta.
- [7] K. Kant, Data center evolution: a tutorial on state of the art, issues, and challenges. *Comput. Network.* 53 (2009) 2939–2965.
- [8] M.J. Ellsworth, G.F. Goth, R.J. Zoodsma, A. Arvelo, L.A. Campbell, W.J. Anderl, An overview of the IBM power 775 supercomputer water cooling system. *J. Electron. Packag.* 134 (2012) 020906.
- [9] D.A. Moore, M. Slaby, T. Cader, K. Regimbal, Hybrid warm water cooled super-computing system. *Thermal and Thermomechanical Phenomena in Electronic Systems (ITherm)*, 15th IEEE Intersociety Conference on. IEEE2016, 2016, pp. 614–618.
- [10] Y.F. Maydanik, S.V. Vershinin, V.G. Pastukhov, S.S. Fried, Loop heat pipes for cooling systems of servers. *IEEE Trans. Compon. Packag. Technol.* 33 (2010) 416–423.
- [11] T. Rouse, Mineral insulating oil in transformers. *IEEE Electr. Insul. Mag.* 14 (1998) 6–16.
- [12] T. Endo, A. Nukada, S. Matsuoka, TSUBAME-KFC: a modern liquid submersion cooling prototype towards exascale becoming the greenest supercomputer in the world. *Parallel and Distributed Systems (ICPADS)*, 20th IEEE International Conference on. IEEE2014, 2014, pp. 360–367.
- [13] M. LaMonica, Intel Servers Take a Deep Dive to Cool off, MIT Technology Reveiw, 2012.
- [14] Ian Cutress, GIGABYTE Server Shows Two-Phase Immersion Liquid Cooling on a 2U GPU G250-S88 using 3M Novec, (2017).
- [15] C. Buffone, Testing of a low-cost loop heat pipe design. *J. Electron. Cool. Therm. Control* (2014) 33–38.
- [16] B.-J. Huang, Y.-H. Chuang, P.-E. Yang, Low-cost manufacturing of loop heat pipe for commercial applications. *Appl. Therm. Eng.* 126 (2017) 1091–1097.
- [17] J. Choi, B. Sung, J. Yoo, C. Kim, D.-A. Borca-Tasciuc, Enhanced miniature loop heat pipe cooling system for high power density electronics. *J. Therm. Sci. Eng. Appl.* 4 (2012) 021008.
- [18] Y. Shabany, *Heat Transfer: thermal Management of Electronics*, CRC Press, 2009.
- [19] C. Tantolin, M. Lallemand, U. Eckes, Experimental study of immersion cooling for power components. *Control, Control'94 International Conference on. IET1994*, 1994, pp. 723–727.
- [20] T. Committee, *Datacom Equipment Power Trends and Cooling Applications*, ASHRAE, Atlanta, GA, 2005.
- [21] Y.-W. Lu, S.G. Kandlikar, Nanoscale surface modification techniques for pool boiling enhancement—a critical review and future directions. *Heat Tran. Eng.* 32 (2011) 827–842.
- [22] S. Mori, Y. Utaka, Critical heat flux enhancement by surface modification in a saturated pool boiling: a review. *Int. J. Heat Mass Tran.* 108 (2017) 2534–2557.
- [23] C. Colin, O. Kannengieser, W. Bergez, M. Lebon, J. Sebilleau, M. Sagan, et al., Nucleate pool boiling in microgravity: recent progress and future prospects. *Compt. Rendus Mec.* 345 (2017) 21–34.
- [24] S. An, D.-Y. Kim, J.-G. Lee, H.S. Jo, M.-w. Kim, S.S. Al-Deyab, et al., Supersonically sprayed reduced graphene oxide film to enhance critical heat flux in pool boiling. *Int. J. Heat Mass Tran.* 98 (2016) 124–130.
- [25] H.S. Jo, J.-G. Lee, S. An, T.G. Kim, S.C. James, J. Choi, et al., Supersonically sprayed, triangular copper lines for pool boiling enhancement. *Int. J. Heat Mass Tran.* 113 (2017) 210–216.
- [26] H.S. Jo, M.-W. Kim, K. Kim, S. An, Y.I. Kim, S.C. James, et al., Effects of capillarity on pool boiling using nanotextured surfaces through electrosprayed BiVO₄ nano-pillars. *Chem. Eng. Sci.* 171 (2017) 360–367.
- [27] H.S. Jo, S. An, H.G. Park, M.-W. Kim, S.S. Al-Deyab, S.C. James, et al., Enhancement of critical heat flux and superheat through controlled wettability of cuprous-oxide fractal-like nanotextured surfaces in pool boiling. *Int. J. Heat Mass Tran.* 107 (2017) 105–111.
- [28] D.-Y. Kim, J.-J. Park, J.-G. Lee, D. Kim, S.J. Tark, S. Ahn, et al., Cold spray deposition of copper electrodes on silicon and glass substrates. *J. Therm. Spray Technol.* 22 (2013) 1092–1102.
- [29] M.S. El-Genk, H. Bostanci, Saturation boiling of HFE-7100 from a copper surface, simulating a microelectronic chip. *Int. J. Heat Mass Tran.* 46 (2003) 1841–1854.
- [30] J.-G. Lee, D.-Y. Kim, B. Kang, D. Kim, H.-e. Song, J. Kim, et al., Nickel–copper hybrid electrodes self-adhered onto a silicon wafer by supersonic cold-spray. *Acta Mater.* 93 (2015) 156–163.
- [31] F.P. Incropera, A.S. Lavine, T.L. Bergman, D.P. DeWitt, *Fundamentals of Heat and Mass Transfer*, Wiley, 2007.
- [32] W.M. Rohsenow, A Method of Correlating Heat Transfer Data for Surface Boiling of Liquids, MIT Division of Industrial Cooperation, [1951], Cambridge, Mass, 1951.
- [33] L.-T. Chen, Heat transfer to pool-boiling Freon from inclined heating plate. *Lett. Heat Mass Tran.* 5 (1978) 111–120.
- [34] J. Holman, Analysis of experimental data. *Experimental methods for engineers* (2001) 48–143.
- [35] B.-U. Hwang, J.-H. Lee, T.Q. Trung, E. Roh, D.-I. Kim, S.-W. Kim, et al., Transparent stretchable self-powered patchable sensor platform with ultrasensitive recognition of human activities. *ACS Nano* 9 (2015) 8801–8810.
- [36] J. Eick, R. Good, A. Neumann, Thermodynamics of contact angles. II. Rough solid surfaces. *J. Colloid Interface Sci.* 53 (1975) 235–248.
- [37] D. Kwok, C. Budziak, A. Neumann, Measurements of static and low rate dynamic contact angles by means of an automated capillary rise technique. *J. Colloid Interface Sci.* 173 (1995) 143–150.
- [38] P. Carman, Fluid flow through granular beds. *Chem. Eng. Res. Des.* 75 (1997) S32–S48.

- [39] G. Brown, The Darcy-weisbach Equation, Oklahoma State University–Stillwater, 2000.
- [40] A. Žukauskas, Heat transfer from tubes in crossflow, *Adv. Heat Tran.* 8 (1972) 93–160.
- [41] S. Whitaker, Forced convection heat transfer correlations for flow in pipes, past flat plates, single cylinders, single spheres, and for flow in packed beds and tube bundles, *AIChE J.* 18 (1972) 361–371.
- [42] S.J. Thiagarajan, R. Yang, C. King, S. Narumanchi, Bubble dynamics and nucleate pool boiling heat transfer on microporous copper surfaces, *Int. J. Heat Mass Tran.* 89 (2015) 1297–1315.
- [43] M.S. El-Genk, J.L. Parker, Enhanced boiling of HFE-7100 dielectric liquid on porous graphite, *Energy Convers. Manag.* 46 (2005) 2455–2481.
- [44] J. Liu, D. Lee, A. Su, Boiling of methanol and HFE-7100 on heated surface covered with a layer of mesh, *Int. J. Heat Mass Tran.* 44 (2001) 241–246.
- [45] C.K. Yu, D.C. Lu, T.C. Cheng, Pool boiling heat transfer on artificial micro-cavity surfaces in dielectric fluid FC-72, *J. Micromech. Microeng.* 16 (2006) 2092.